

RESEARCH ARTICLE

On the strength of transversely isotropic rocks

Yang Zhao | Shabnam J. Semnani | Qing Yin | Ronaldo I. Borja 

Department of Civil and Environmental Engineering, Stanford University, Stanford, CA 94305, USA

Correspondence

Ronaldo I. Borja, Department of Civil and Environmental Engineering, Stanford University, Stanford, CA 94305, USA.
Email: borja@stanford.edu

Summary

Accurate prediction of strength in rocks with distinct bedding planes requires knowledge of the bedding plane orientation relative to the load direction. Thermal softening adds complexity to the problem since it is known to have significant influence on the strength and strain localization properties of rocks. In this paper, we use a recently proposed thermoplastic constitutive model appropriate for rocks exhibiting transverse isotropy in both the elastic and plastic responses to predict their strength and strain localization properties. Recognizing that laboratory-derived strengths can be influenced by material and geometric inhomogeneities of the rock samples, we consider both stress-point and boundary-value problem simulations of rock strength behavior. Both plane strain and 3D loading conditions are considered. Results of the simulations of the strength of a natural Tournemire shale and a synthetic transversely isotropic rock suggest that the mechanical model can reproduce the general U-shaped variation of rock strength with bedding plane orientation quite well. We show that this variation could depend on many factors, including the stress loading condition (plane strain versus 3D), degree of anisotropy, temperature, shear-induced dilation versus shear-induced compaction, specimen imperfections, and boundary restraints.

KEYWORDS

anisotropy, bifurcation, rock strength, shear band, thermoplasticity, transverse isotropy

1 | INTRODUCTION

Anisotropy is a ubiquitous property of natural rocks.¹⁻¹² Transverse isotropy is a particular type of anisotropy that arises from the existence of bedding planes. Transverse isotropy is defined by a plane of isotropy (ie, the bedding plane) and an axis of anisotropy (ie, the normal to the bedding plane). It is generally recognized that the strength of a transversely isotropic rock depends on the direction of load relative to the bedding plane. Maximum load applied in the bed-parallel direction could differ appreciably from the maximum load applied in the bed-normal direction. But what happens in between is a more intriguing feature of anisotropic rock behavior: The strength degrades from the smaller of the bed-parallel and bed-normal values until it reaches a minimum at a critical bedding plane orientation, then rises until it reaches the larger of the 2 end strengths, thus forming an asymmetric U-shaped curve when plotted against the bedding plane orientation. Therefore, in describing the strength of a transversely isotropic rock, it is not sufficient to simply quantify the maximum load that can be applied in either the bed-parallel or bed-normal direction. What is more important is to determine the critical orientation of the bedding plane relative to the load and predict what value the strength degrades to at this critical orientation.

Numerous investigators have conducted laboratory tests to quantify the microstructure and investigate the effect of anisotropy on strength of various transversely isotropic rocks, such as Martinsburg slate,¹³ South African slate,¹⁴ Penrhyn slate,¹⁵ Green River shale,¹⁶ Tournemire shale,^{17,18} phyllites,¹⁹ schist,²⁰ Woodford shale,²¹⁻²³ and synthetic transversely isotropic rocks.²⁴ Triaxial compression testing under various confining pressures is one of the most common methods used to measure the strength of rock samples. For transversely isotropic rocks, it is vastly reported in the literature that rock strength obtained from triaxial tests is dependent on the bedding plane orientation in the test samples, exhibiting an asymmetric U-shaped variation with respect to the orientation of bedding planes. Higher confining pressure generally leads to a more ductile behavior and reduction in the strength anisotropy.²⁵

To describe the dependence of strength on bedding plane orientation for transversely isotropic rocks, researchers have proposed several failure criteria, which can be divided into 3 main categories,²⁶ namely, discontinuous, empirical, and mathematical criteria. The discontinuous criteria associate failure with fractures of rock matrix or bedding planes.^{25,27-29} Jaeger²⁸ introduced the single plane of weakness theory by generalization of the Coulomb-Navier criterion for rocks, assuming 2 failure modes, namely, sliding along the weak plane and failure across the rock matrix. Tien and Kuo²⁵ proposed a failure criterion by extending Jaeger's criterion and using Hoek-Brown model³⁰ instead of Mohr-Coulomb to fit experimental data for both brittle and ductile regions. Their model was later applied to synthetic transversely isotropic rocks.²⁴

The second approach is based on deriving empirical relations for variation of material parameters with the loading orientation.^{16,30-32} The first model of this kind was proposed by Jaeger,³³ who extended the Mohr-Coulomb criterion by deriving empirical equations for variation of material cohesion with bedding plane orientation. McLamore and Gray¹⁶ extended Jaeger's criterion by using variable material cohesion and friction coefficients with the bedding plane orientation. Hoek and Brown³⁰ developed an anisotropic failure criterion for transversely isotropic rocks based on their famous isotropic Hoek-Brown criterion. They incorporated anisotropy into the model by assuming that the constants in the isotropic criterion vary with the bedding plane orientation. Hoek-Brown model was also modified later by Saroglou and Tsiambaos³² by introducing a new parameter to account for strength anisotropy.

Empirical models could illustrate the influence of bedding plane on strength of typical transversely isotropic rocks with acceptable accuracy. However, the validity of such models is restricted to a limited data set. Parameters used in such criteria have little physical significance, as they only try to reproduce the U-shaped variation between rock strength and bedding plane orientation; therefore, they may be inapplicable to cases dominated by other physical effects. It must be noted that both discontinuous and empirical models focus on providing the strength at failure, but not necessarily the constitutive behavior of the material.

A more meaningful way to take bedding plane effects into consideration is to incorporate anisotropy directly into the constitutive law. In this case, the stress-strain response itself will vary with the bedding plane orientation, which will then result in the dependence of rock strength on the bedding plane orientation. For elasto-plastic models, the key concept is to find the yield criterion that contains anisotropy. Gol'denblat and Kopnov³⁴ proposed a general expression of yield criterion as a polynomial of stress components to model glass-reinforced plastics. As a subset of this, Tsai and Wu³⁵ proposed a yield criterion as a polynomial that only contains linear and quadratic terms of stress components to model filamentary composites.

Other than finding a general expression, a vast majority of the anisotropic plasticity models are based on extending the existing isotropic criteria. Pioneering works in this area include the work by Hill,³⁶ who extended the von Mises criterion, and Pariseau,³⁷ who extended the Mohr-Coulomb criterion, to account for anisotropy. Boehler and Sawczuk³⁸ also proposed an approach to take advantage of isotropic models directly, by projecting stress into an alternative stress space using a fourth order tensor, and replacing the alternative stress tensor into isotropic yield criterion. Based on this concept, Nova³⁹ extended the Cam-Clay model, and Crook et al⁴⁰ extended the modified Cam-Clay model for transversely isotropic rocks. An overview of anisotropic plasticity models can be found in Semnani et al.⁴¹ Grain-scale models explaining the origin of anisotropy include those developed in other studies.⁴²⁻⁴⁵

Laboratory investigations reveal that temperature changes influence the mechanical behavior of rocks and soils.⁴⁶⁻⁴⁸ Masri et al⁴⁷ investigated the effect of temperature on the mechanical behavior of Tournemire shale, revealing that the rock strength will decrease, and the deformation of rock will be more ductile with the increase of temperature. They also reported that temperature will influence the anisotropic response related to the deformation of bedding planes. To take thermal effects into account, researchers have proposed a variety of thermoplasticity models. Among them, Hueckel and Borsetto⁴⁹ and Graham et al⁵⁰ coupled the isotropic MCC model with thermal effects to illustrate the mechanical behaviors of shale and clays.

This paper builds upon the thermo-elastoplastic constitutive model presented by Semnani et al⁴¹ and provides an in-depth investigation into the aforementioned variation of rock strength with bedding plane orientation. Plastic anisotropy is represented by a rotated ellipsoidal yield surface of modified Cam-Clay model, developed specifically to accommodate transverse isotropy, and is enhanced further to include thermal softening. Novel contributions of the present work include insight into strength that develops when loading on the compaction and dilation sides of the yield surface, with and without thermal effects. Most of the analyses involve 3D simulations since the bedding plane geometry naturally creates 3D effects (even if the imposed loading is axisymmetric, for example).

In addition to the stress-point simulations, boundary-value problems are also solved to show the impact of imperfection and boundary restraints on the strength of a rock sample. Note that the studies of Semnani et al⁴¹ were restricted to stress-point simulations and did not include simulation of boundary-value problems. Results of the present work reveal that simulations of boundary-value problems could provide vastly different insights into the localization properties of rocks. For example, we show that boundary restraints could induce plastic strain localization in bed-parallel direction even if the material wanted to bifurcate into a shear band in the bed-normal direction. This could provide mechanistic explanations for the development of a zigzagging failure zone in rocks with distinct bedding planes, a pattern in which the localization zone jumps from one bedding plane to another bedding plane.²⁴

2 | CONSTITUTIVE THEORY

As a mathematical representation of the yield function, we consider the tensorial operators \otimes , \oplus , and \ominus defined such that $(\bullet \otimes \circ)_{ijkl} = (\bullet)_{ij}(\circ)_{kl}$, $(\bullet \oplus \circ)_{ijkl} = (\bullet)_{jl}(\circ)_{ik}$, and $(\bullet \ominus \circ)_{ijkl} = (\bullet)_{il}(\circ)_{jk}$. Let \mathbf{n} denote the unit normal to bedding plane; the second-order microstructure tensor \mathbf{m} is defined as follows:

$$\mathbf{m} = \mathbf{n} \otimes \mathbf{n}. \quad (1)$$

Following Semnani et al,⁴¹ we perform a linear map of the Cauchy stress tensor $\boldsymbol{\sigma}$ in real space to the Cauchy stress tensor $\boldsymbol{\sigma}^*$ in fictitious space via a projection tensor \mathbb{P} . The mapping takes the form

$$\boldsymbol{\sigma}^* = \mathbb{P} : \boldsymbol{\sigma}, \quad (2)$$

where

$$\mathbb{P} = c_1 \mathbb{I} + \frac{c_2}{2} (\mathbf{m} \oplus \mathbf{m} + \mathbf{m} \ominus \mathbf{m}) + \frac{c_3}{4} (\mathbf{1} \oplus \mathbf{m} + \mathbf{m} \oplus \mathbf{1} + \mathbf{1} \ominus \mathbf{m} + \mathbf{m} \ominus \mathbf{1}), \quad (3)$$

c_1 , c_2 , and c_3 are the anisotropy parameters, $\mathbf{1}$ is the second-order identity tensor (Kronecker delta), and \mathbb{I} is the rank-four symmetric identity tensor. The purpose of this transformation is to map an anisotropic yield function $f(\boldsymbol{\sigma})$ in real space to its isotropic form $f_{iso}(\boldsymbol{\sigma}^*)$ in fictitious space, ie,

$$f(\boldsymbol{\sigma}) = f_{iso}(\boldsymbol{\sigma}^*). \quad (4)$$

More specifically, we consider in this paper a rotated modified Cam-Clay yield function⁵¹ whose form in the fictitious space is given by the isotropic function

$$f_{iso}(\boldsymbol{\sigma}^*, p_c) = \frac{q^{*2}}{2M^2} + p^*(p^* - p_c) \leq 0, \quad (5)$$

where $p^* = \text{tr}(\boldsymbol{\sigma}^*)/3$, $q^* = \sqrt{3/2} \|\mathbf{s}^*\|$, $\mathbf{s}^* = \boldsymbol{\sigma}^* - p^* \mathbf{1}$, M is the slope of the critical state line, and p_c is a state variable more commonly known as the preconsolidation pressure. In real space, the form of the anisotropic yield function is given by

$$f(\boldsymbol{\sigma}, p_c) = \frac{\|\boldsymbol{\sigma}\|_{\mathbb{A}^*}}{2M^2} + (\mathbf{a}^* : \boldsymbol{\sigma})(\mathbf{a}^* : \boldsymbol{\sigma} - p_c) \leq 0, \quad (6)$$

where

$$\mathbf{a}^* = \frac{1}{3} \mathbb{P} : \mathbf{1}, \quad \|\boldsymbol{\sigma}\|_{\mathbb{A}^*} = \sqrt{\boldsymbol{\sigma} : \mathbb{A}^* : \boldsymbol{\sigma}}, \quad (7)$$

and

$$\mathbb{A}^* = 3\mathbb{P} : \left(\mathbb{I} - \frac{1}{3} \mathbf{1} \otimes \mathbf{1} \right) : \mathbb{P}. \quad (8)$$

Note that the rotation of the yield surface is determined by the orientation of the bedding plane.

We consider a thermo-mechanical hardening law of the form

$$p_c = p_{c0} \exp\left(\frac{\epsilon_v^p}{\lambda^p}\right) \mathcal{G}(\Theta), \quad (9)$$

where ϵ_v^p is the plastic volumetric strain, p_{c0} is a reference preconsolidation pressure, λ^p is a compressibility parameter, and $\mathcal{G}(\Theta)$ is a thermal softening law that varies with absolute temperature Θ . In this paper, we use the Laloui and Cekerevac⁵² thermal softening law:

$$\mathcal{G}(\Theta) = \left[1 - \gamma_T \ln\left(1 + \frac{\Delta\Theta}{\Theta_0 - 273}\right) \right], \quad (10)$$

where γ_T is a material softening parameter. Employing the associative flow rule gives $\delta\epsilon_v^p < 0$ on the dilation side, suggesting that the plastic-induced softening is amplified by thermal softening. On the other hand, $\delta\epsilon_v^p > 0$ on the compression side, which means that the plastic-induced hardening is now in competition with thermal softening. These 2 effects play important roles in determining the strength of transversely isotropic rocks.

Cross-anisotropy also impacts the elastic response. For a transversely isotropic hyperelastic material, we assume the following quadratic form of the elastic stored energy function

$$\Psi(I_1, I_2, I_3, I_4, I_5) = \frac{1}{2}\lambda I_1^2 + \mu_T I_2 + a I_1 I_4 + \frac{1}{2}b I_4^2 + 2(\mu_L - \mu_T) I_5, \quad (11)$$

where a , b , μ_T , μ_L , and λ are material parameters representing the mechanical properties of the material, and

$$\begin{aligned} I_1 &= \text{tr}(\boldsymbol{\epsilon}), & I_2 &= \text{tr}(\boldsymbol{\epsilon}^2), & I_3 &= \text{tr}(\boldsymbol{\epsilon}^3), \\ I_4 &= \text{tr}(\boldsymbol{\epsilon} \cdot \mathbf{m}), & I_5 &= \text{tr}(\boldsymbol{\epsilon}^2 \cdot \mathbf{m}) \end{aligned} \quad (12)$$

are 5 invariants. Note that I_1 , I_2 , and I_3 are invariants of $\boldsymbol{\epsilon}$, which capture the isotropic effect, whereas I_4 and I_5 represent the effect of cross-anisotropy. Differentiating Ψ twice with respect to $\boldsymbol{\epsilon}$ yields a tensorial expression for the elastic tangent modulus for a transversely isotropic material,

$$\begin{aligned} \mathbb{C}^e &= \lambda \mathbf{1} \otimes \mathbf{1} + 2\mu_T \mathbb{I} + a(\mathbf{1} \otimes \mathbf{m} + \mathbf{m} \otimes \mathbf{1}) + b \mathbf{m} \otimes \mathbf{m} \\ &+ (\mu_L - \mu_T)(\mathbf{1} \oplus \mathbf{m} + \mathbf{m} \oplus \mathbf{1} + \mathbf{1} \ominus \mathbf{m} + \mathbf{m} \ominus \mathbf{1}). \end{aligned} \quad (13)$$

Note that the elastic response is defined by 5 constants in this case.

3 | NUMERICAL IMPLEMENTATION

In what follows, all state variables with subscript n denote known values at time t_n ; variables without a subscript denote unknown values at time t_{n+1} . The objective of the computation is to march the solution in time by calculating the values of the state variables at time t_{n+1} given their values at time t_n and the imposed incremental strain tensor $\Delta\boldsymbol{\epsilon}$.

The equations to satisfy include the update equation for the elastic strain component of the strain tensor,

$$\boldsymbol{\epsilon}^e = \boldsymbol{\epsilon}^{e\text{tr}} - \Delta\lambda \frac{\partial f}{\partial \boldsymbol{\sigma}}, \quad (14)$$

where $\boldsymbol{\epsilon}^{e\text{tr}} = \boldsymbol{\epsilon}_n^e + \Delta\boldsymbol{\epsilon} + \alpha_t(\Theta - \Theta_n)\mathbf{1}$ is the trial elastic strain tensor, $\boldsymbol{\sigma} = \mathbb{C}^e : \boldsymbol{\epsilon}^e$ is the elastic constitutive equation, and $\Delta\lambda$ is the discrete consistency parameter. In addition, the hardening/softening law in the plastic regime takes the form

$$p_c = p_{c0} \exp\left(\frac{\epsilon_v^p}{\lambda^p}\right) \left[1 - \gamma_T \ln\left(1 + \frac{\Delta\Theta}{\Theta_0 - 273}\right) \right], \quad (15)$$

where $\epsilon_v^p = \text{tr}(\boldsymbol{\epsilon}^p) = \text{tr}(\boldsymbol{\epsilon}) - \text{tr}(\boldsymbol{\epsilon}^e)$ and $\boldsymbol{\epsilon}$ is given. The discrete consistency condition in the plastic regime takes the form

$$f(\boldsymbol{\sigma}, p_c) = 0. \quad (16)$$

We can view the above 3 equations as a nonlinear system in the unknowns $\boldsymbol{\epsilon}^e$, $\Delta\lambda$, and p_c . One way of solving this system of equations is to treat them monolithically under one Newton iteration loop and solve for the unknowns simultaneously.⁵¹ Alternatively, we can solve smaller systems of equation under multiple Newton iteration loops. We employ the latter approach in what follows.

Consider ϵ^e and p_c as functions of $\Delta\lambda$. Here, we take $\Delta\lambda$ as our major variable. We can solve the discrete consistency condition for $\Delta\lambda$ as follows:

$$r(\Delta\lambda) = f(\boldsymbol{\sigma}, p_c) \rightarrow 0. \quad (17)$$

The tangent operator can be readily evaluated as follows:

$$r'(\Delta\lambda) = \frac{\partial f}{\partial \boldsymbol{\sigma}} : \mathbb{C}^e : \frac{\partial \epsilon^e}{\partial \Delta\lambda} + \frac{\partial f}{\partial p_c} \frac{\partial p_c}{\partial \Delta\lambda}. \quad (18)$$

The individual partial derivatives are given below:

$$\frac{\partial f}{\partial \boldsymbol{\sigma}} = \frac{1}{M^2} \mathbb{A}^* : \boldsymbol{\sigma} + (2p^* - p_c) \mathbf{a}^* \quad (19)$$

and

$$\frac{\partial \epsilon^e}{\partial \Delta\lambda} = - \left(\mathbb{I} + \Delta\lambda \frac{\partial^2 f}{\partial \boldsymbol{\sigma} \partial \epsilon^e} \right)^{-1} : \frac{\partial f}{\partial \boldsymbol{\sigma}}, \quad (20)$$

where

$$\frac{\partial^2 f}{\partial \boldsymbol{\sigma} \partial \epsilon^e} = \frac{\mathbb{A}^* : \mathbb{C}^e}{M^2} + 2\mathbf{a}^* \otimes \mathbf{a}^* : \mathbb{C}^e + \frac{p_c}{\lambda^p} \mathbf{a}^* \otimes \mathbf{1}. \quad (21)$$

The remaining derivatives are

$$\frac{\partial f}{\partial p_c} = -p^* \quad (22)$$

and

$$\frac{\partial p_c}{\partial \Delta\lambda} = -\frac{p_c}{\lambda^p} \mathbf{1} : \frac{\partial \epsilon^e}{\partial \Delta\lambda}. \quad (23)$$

The elastic strain tensor ϵ^e is not an explicit function of $\Delta\lambda$, so it must be solved iteratively. To this end, we define another residual tensor function

$$\boldsymbol{\rho}(\epsilon^e) = \epsilon^e - \epsilon^{e\text{tr}} + \Delta\lambda \frac{\partial f}{\partial \boldsymbol{\sigma}} \rightarrow \mathbf{0}. \quad (24)$$

The tangent operator in this case takes the form

$$\boldsymbol{\rho}'(\epsilon^e) = \mathbb{I} + \Delta\lambda \frac{\partial^2 f}{\partial \boldsymbol{\sigma} \partial \epsilon^e}, \quad (25)$$

where the second partial derivative term is obtained from (21).

Box 1 shows the algorithm for solving $\Delta\lambda$. The algorithm consists of 2 Newton iteration loops: an outer loop to solve for $\Delta\lambda$, and an inner loop to solve for ϵ^e . While a single iteration loop to solve for both variables may look simpler at first glance, we note that we are solving the full strain tensor ϵ^e and not just its invariants, unlike in the isotropic case, since anisotropy does not preserve the coaxiality of the stress and elastic strain tensors.⁵¹ So the reduction in size of the residual vector $\boldsymbol{\rho}$ is a welcome means to alleviate the computational burden.

Step 1. Initialize $k = 0$:

$$\Delta\lambda^k = 0, r^k(0), \boldsymbol{\sigma}^k = \boldsymbol{\sigma}_n, p_c^k = p_{cn} \mathcal{G}(\boldsymbol{\Theta}) / \mathcal{G}(\boldsymbol{\Theta}_n), \epsilon^{ek} = \epsilon_n^e.$$

Step 2. Inner loop: Compute ϵ^{ek} for a given $\Delta\lambda^k$.

Step 3. Compute $\boldsymbol{\sigma}^k = \mathbb{C}^e : \epsilon^{ek}$ and p_c^k from hardening law.

Step 4. Compute $A_k = -r'(\Delta\lambda^k)$.

Step 5. Update $\Delta\lambda^{k+1} = \Delta\lambda^k + A_k^{-1} r^k(\Delta\lambda^k)$ and $r^{k+1} = r(\Delta\lambda^{k+1})$.

Step 6. $k \leftarrow k + 1$.

Step 7. If $|r^k| < \text{tol}$, update $\boldsymbol{\Theta}_{n+2} = \boldsymbol{\Theta} + \zeta \boldsymbol{\sigma} : (\epsilon^p - \epsilon_n^p) / \rho_c$, exit;

Else, go to Step 2.

Box 1. Stress-point integration for transversely isotropic constitutive model.

Next, we evaluate the algorithmic tangent operator for the finite element problem. To this end, we now regard the 2 variables, ϵ^e and $\Delta\lambda$, as functions of the prescribed total strain ϵ , ie,

$$\epsilon^e = \epsilon^e(\epsilon), \quad \Delta\lambda = \Delta\lambda(\epsilon). \quad (26)$$

The algorithmic tangent operator can then be evaluated from the chain rule as follows:

$$\mathbb{C} = \frac{\partial \sigma}{\partial \epsilon} = \frac{\partial \sigma}{\partial \epsilon^e} : \frac{\partial \epsilon^e}{\partial \epsilon} = \mathbb{C}^e : \frac{\partial \epsilon^e}{\partial \epsilon}. \quad (27)$$

To derive the expression for $\partial \epsilon^e / \partial \epsilon$, we need to take advantage of the invariance of the residuals r and ρ for both the outer loop and inner loop, respectively, with respect to ϵ .

For the outer loop, we note that

$$r = f(\sigma(\epsilon^e), p_c(\epsilon^e, \epsilon)) = 0 \quad (28)$$

after the local iterations have converged. Thus, $\partial r / \partial \epsilon = \mathbf{0}$ at the locally converged state, or

$$\frac{\partial f}{\partial \sigma} : \mathbb{C}^e : \frac{\partial \epsilon^e}{\partial \epsilon} + \frac{\partial f}{\partial p_c} \frac{\partial p_c}{\partial \epsilon} + \frac{\partial f}{\partial p_c} \frac{\partial p_c}{\partial \epsilon^e} : \frac{\partial \epsilon^e}{\partial \epsilon} = \mathbf{0}. \quad (29)$$

This yields

$$\left(\frac{\partial f}{\partial \sigma} : \mathbb{C}^e + \frac{p_c p^*}{\lambda^p} \mathbf{1} \right) : \frac{\partial \epsilon^e}{\partial \epsilon} = \frac{p_c p^*}{\lambda^p} \mathbf{1}. \quad (30)$$

For the inner loop, on the other hand, we also note that ρ is also zero at the locally converged state, and thus, $\partial \rho / \partial \epsilon = \mathbf{0}$, or

$$\frac{\partial \epsilon^e}{\partial \epsilon} - \mathbb{I} + \frac{\partial f}{\partial \sigma} \otimes \frac{\partial \Delta\lambda}{\partial \epsilon} + \Delta\lambda \frac{\partial^2 f}{\partial \sigma \partial \epsilon} = \mathbf{0}. \quad (31)$$

This yields

$$\left(\mathbb{I} + \Delta\lambda \frac{\partial^2 f}{\partial \sigma \partial \epsilon} \right) : \frac{\partial \epsilon^e}{\partial \epsilon} + \frac{\partial f}{\partial \sigma} \otimes \frac{\partial \Delta\lambda}{\partial \epsilon} = \mathbb{I} + \frac{p_c \Delta\lambda}{\lambda^p} \mathbf{a}^* \otimes \mathbf{1}, \quad (32)$$

after noting that

$$\frac{\partial^2 f}{\partial \sigma \partial \epsilon} = \frac{\partial^2 f}{\partial \sigma \partial \epsilon^e} : \frac{\partial \epsilon^e}{\partial \epsilon} - \frac{p_c}{\lambda^p} \mathbf{a}^* \otimes \mathbf{1}. \quad (33)$$

Equations 30 and 32 can be solved simultaneously for the unknowns $\partial \epsilon^e / \partial \epsilon$ and $\partial \Delta\lambda / \partial \epsilon$, although in our case, only the former expression is needed.

4 | STRESS-POINT SIMULATIONS

In this section, we conduct stress-point simulations to investigate the variation of strength of transversely isotropic rocks with bedding plane orientation. In the present work, we define “strength” based on 3 possible criteria: (1) stress at initial yield (for overconsolidated rocks), (2) stress at peak point, and (3) stress at the onset of shear band deformation⁵³ according to the criterion of Rudnicki and Rice⁵⁴ for isothermal deformation, and Semnani et al⁴¹ for adiabatic condition. We validate the formulation using data for Tournemire shale^{18,41} and for a synthetic transversely isotropic rock²⁴ under 3D loading conditions, in both isothermal and adiabatic conditions. We note at the outset that triaxial tests cannot be represented as a 2D axisymmetric problem owing to the added dimension introduced by an inclined bedding plane.

4.1 | Tournemire shale

Stress-strain data from triaxial tests on Tournemire shale have been reported by Niandou et al.¹⁸ In this work, we simulate their tests as a 3D problem in which the 2 principal stresses in the horizontal direction are the same as the confining pressure and the axial strain is increasing. We note that Semnani et al⁴¹ conducted hypothetical plane strain simulations on this rock without adopting the parameters calibrated via the actual tests conducted under triaxial stress conditions. Here, we calibrate the material parameters for this shale directly from the triaxial test data of Niandou et al¹⁸ for 40 MPa confining pressure, making the present simulations more in sync with reality.

The calibrated parameters for elasticity are $a = -1870$ MPa, $b = 5420$ MPa, $\lambda = 4270$ MPa, $\mu_L = 6510$ MPa, and $\mu_T = 9360$ MPa. These parameters are based on the tensorial representation for \mathbb{C}^e given in Section 2. In terms of the matrix representation used by Semnani et al,⁴¹ the equivalent elasticity parameters are $E_1 = 12860$ MPa, $E_2 = 21900$ MPa, $\nu_{12} = 0.15$, $\nu_{23} = 0.17$, and $G_{12} = 6510$ MPa. The parameters for plasticity are $M = 1.07$, $\lambda^p = 0.0026$, $c_1 = 0.7$, $c_2 = -0.36$, and $c_3 = 0.6$. In terms of the representation used by Semnani et al,⁴¹ the aforementioned values of c_1 , c_2 , and c_3 are equivalent to the anisotropy parameters $\alpha = 0.94$, $\beta = 0.7$, and $\gamma = 1.0$. We remark that the material parameters used in the paper by Semnani et al⁴¹ were only hypothetical values and not based on the triaxial test data of Niandou et al.¹⁸

Following the test procedure described by Niandou et al,¹⁸ we first subject the rock sample to an initial confining pressure of 40 MPa, which equals the initial preconsolidation pressure p_c for a normally consolidated rock, and then load the sample by increasing the axial compressive strain while holding the 2 lateral stresses fixed. Under isothermal condition, the rock undergoes strain hardening during the loading stage. The stress-strain curve exhibits an asymptote as the stress-point approaches the critical state line. The rock does not strain-soften in this case, and no shear band forms. Thus, the “strength” of the rock may be defined as the asymptotic maximum principal stress difference, which is plotted in Figure 1 as a function of bedding plane orientation θ . Here, $\theta = 0$ corresponds to a horizontal bedding plane, whereas $\theta = 90^\circ$ corresponds to a vertical bedding plane. Observe that the experimentally obtained U-shaped variation is approximately captured by the model, including the fact that the left shoulder at $\theta = 0$ is lower than the right shoulder at $\theta = 90^\circ$, which implies a higher strength in the bed-parallel direction than in the bed-normal direction. This could be due to additional bending mechanism on the clay particles that reduces the strength (and stiffness) of the rock when loaded in the bed-normal direction.

We next investigate the impact of thermal softening on the stress-strain-strength responses by assuming adiabatic condition. In this case, plastic deformation is converted into heat that is confined within the system, thus causing the temperature within the rock sample to increase. This temperature increase produces a softening response, which acts in competition with shear-induced compaction that creates a hardening response.^{55,56} In the following simulations, we assume the following material parameters for thermal effects: $\alpha_t = 10^{-5}/^\circ\text{K}$, $\rho = 2700$ kg/m³, $\theta_0 = 298^\circ\text{K}$, and $c = 7.0$ J/ $^\circ\text{K}\cdot\text{kg}$. Because the plastic strain for the problem is small, a relative small value of c has been chosen to magnify and better illustrate the impact of thermal effects. We then vary the thermal softening parameter γ_T to see how it impacts the resulting stress-strain-strength responses.

Starting with the same initial confining pressure of 40 MPa, the rock sample is then loaded to failure by increasing the axial compressive strain under adiabatic condition. Typical stress-strain responses for different values of γ_T are shown in Figure 2 for bedding plane orientation $\theta = 45^\circ$. Observe that for smaller values of γ_T , significant deformation is needed for thermal softening to overcome the hardening induced by volumetric compaction. In general, thermal softening decreases the maximum principal stress difference and promotes shear band bifurcation (see other works^{41,53,57,58}). The results for different bedding plane orientations are summarized in Figure 3. As expected, thermal softening during adiabatic loading

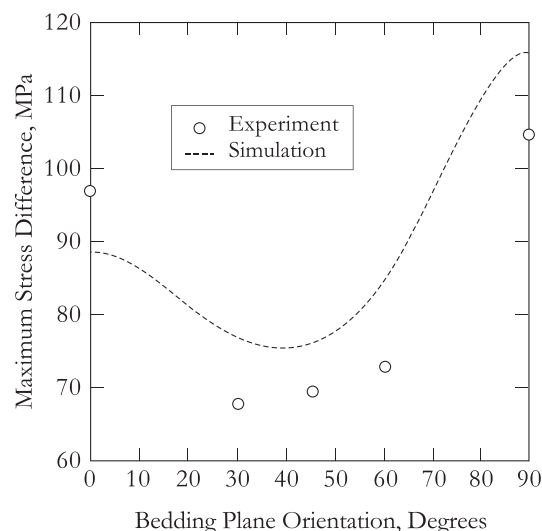


FIGURE 1 Triaxial compression of normally consolidated Tournemire shale: variation of maximum principal stress difference versus bedding plane orientation θ . After Niandou et al¹⁸

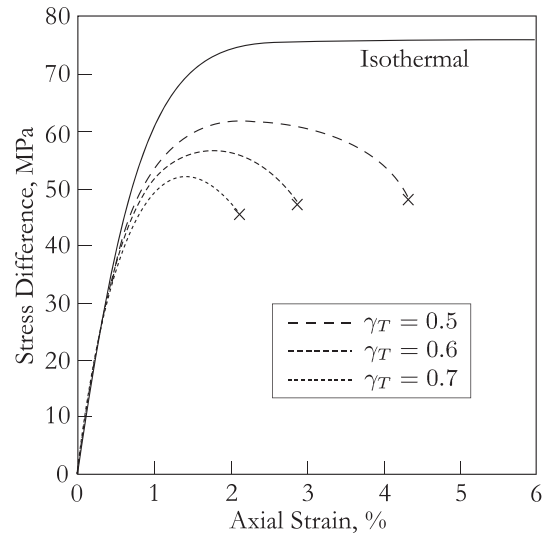


FIGURE 2 Triaxial compression of normally consolidated Tournemire shale: stress-strain responses for bedding plane orientation $\theta = 45^\circ$. Symbol \times denotes shear band bifurcation points

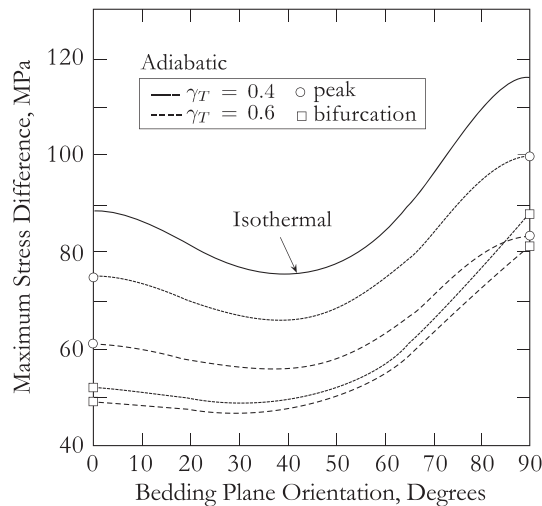


FIGURE 3 Triaxial compression of normally consolidated Tournemire shale: variation of maximum principal stress difference with bedding plane orientation θ under isothermal and adiabatic conditions

tends to reduce the rock strength; however, we see that it also flattens the left shoulder of the U-shaped curve. Furthermore, because the shear band forms in the softening regime, the bifurcation strength is lower than the peak strength. However, it also appears from Figure 3 that the bifurcation strength is not affected by thermal softening as much as the peak strength.

A hypothetical question arises as to what would be the shape of the curve describing the rock strength as a function of bedding plane orientation if the rock was loaded on the dilative side of the yield surface. The rock can load on the dilative side if the initial preconsolidation pressure p_c is much higher than the initial confining pressure σ_c , ie, the rock is overconsolidated. This means that there is a significant elastic response prior to initial yield depending on the degree of overconsolidation of the rock. Because of the form of the hardening/softening law, a dilative plastic volume change results in a softening response even under isothermal condition. Thus, we employ herein two criteria for rock strength when loading on the dilative side, namely, (1) stress at initial yield, and (2) stress at bifurcation point.

To generate an overconsolidated rock, we prescribe an initial preconsolidation pressure of 40 MPa and subject the rock to an initial confining pressure of 1 MPa, so that the overconsolidation ratio is 40. We then load the rock to failure under isothermal condition. Figures 4 and 5 show hypothetical U-shaped curves generated for triaxial and plane strain conditions, respectively. Note that the right shoulder is now much higher than the left shoulder. For the triaxial simulation,

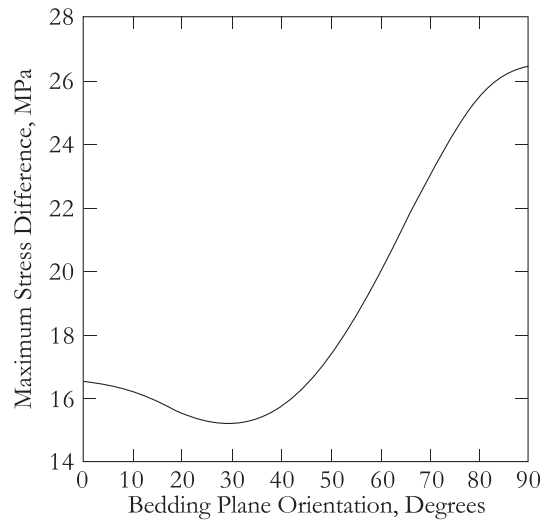


FIGURE 4 Triaxial compression of overconsolidated Tournemire shale: variation of maximum stress difference with bedding plane orientation θ . Initial yield and peak stresses coincide

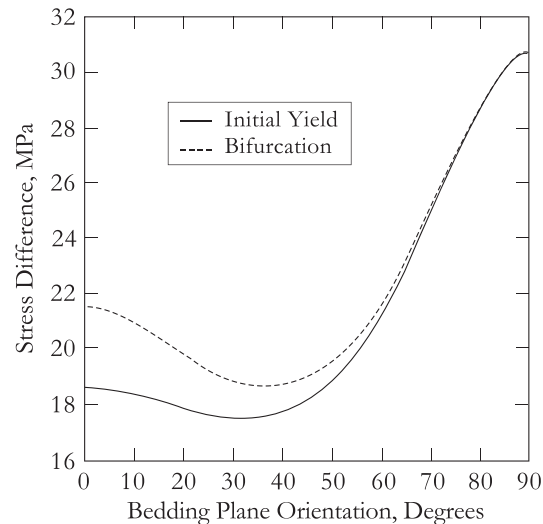


FIGURE 5 Plane strain compression of overconsolidated Tournemire shale: variation of maximum stress difference with bedding plane orientation θ . Peak stresses and bifurcation points coincide

the rock undergoes strain softening at initial yield, although no shear band bifurcation is detected; thus, only one curve is plotted in Figures 4. For the plane strain simulation, the initial yield points do not coincide with the peak stress, but the peak stress coincides with the onset of shear band bifurcation, producing the 2 curves shown in Figures 5. For the plane strain simulation, we have also investigated the relationship between the shear band angle ψ and bedding plane orientation θ , as shown in Figures 6. From this result, we see that the shear band generally crosses the bedding plane nearly at right angle. We should emphasize that these results pertain to the stress-point (constitutive) response and not to the structural response of the rock sample. Thus, they do not account for the effect of material and/or geometric imperfections.

4.2 | Synthetic transversely isotropic rock

Synthetic rocks are rock-like materials made of sand, clay, plaster, cement, resin, and polymers that are mixed together to produce a new material whose properties are similar to those of natural rocks. Tien et al²⁴ varied the weight ratios of cement, kaolinite, and water to produce 2 synthetic rock materials, one with higher strength and stiffness, and the other

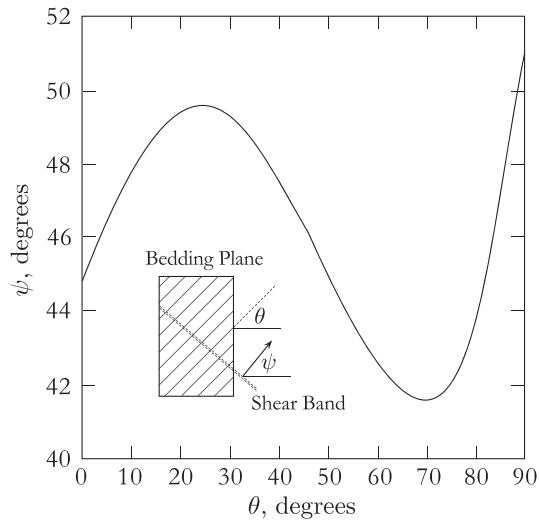


FIGURE 6 Relationship between bedding plane orientation θ and shear band angle ψ for plane strain simulations

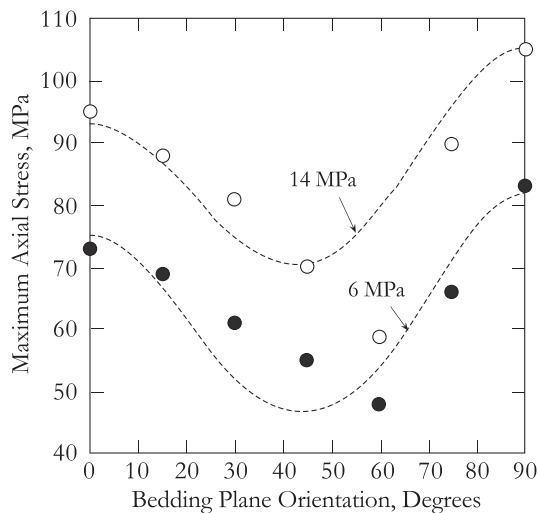


FIGURE 7 Triaxial compression of synthetic transversely isotropic rocks at 6 and 14 MPa confining pressures. After Tien et al²⁴

with lower strength and stiffness. They then layered these two materials in alternating fashion to produce a synthetic transversely isotropic rock, with the plane of each layer representing the plane of isotropy.

In this section, we model the synthetic transversely isotropic rock of Tien et al²⁴ by layering two different materials in alternating fashion: Material #1 with Young's modulus $E = 21700$ MPa and Poisson's ratio $\nu = 0.23$; and Material #2 with $E = 11900$ MPa and $\nu = 0.21$. We take each layer to have the same thickness so that the thickness ratio is 1:1 between the 2 materials. If the representative elementary volume is large enough, we can assume that the bedding plane effect is homogeneous at every point inside the homogenized transversely isotropic rock. For such a synthetic layered rock, we can use the Backus average⁵⁹ to calculate the effective elastic tangent, as illustrated in Appendix A.

For the plasticity component of the constitutive model, we calibrate the parameters at 2 confining pressures: (1) for confining pressure of 6 MPa, we take $M = 2.0$, $\lambda^p = 0.0026$, $\alpha = 0.85$, and $\beta = 0.82$; and (2) for confining pressure of 14 MPa, we take $M = 1.65$, $\lambda^p = 0.0026$, $\alpha = 0.87$, and $\beta = 0.79$; where α and β are the anisotropy parameters of Semnani et al.⁴¹ The slight decrease in the value of M at a higher confining pressure reflects the fact that the critical state line may curve slightly downwards with higher confining pressure. Apart from this, the anisotropy parameters are essentially the same for the 2 confining pressures. Assuming isothermal condition and a normally consolidated rock, Figure 7 shows the constitutive model reproducing the experimentally derived U-shaped variations of rock strength with bedding plane orientation at these 2 confining pressures quite well.

5 | BOUNDARY-VALUE PROBLEMS

This section provides a mechanistic explanation for why failure zones in rocks with distinct bedding planes tend to zigzag along and across the bedding planes when loaded in compression. The discussion highlights the importance of end restraints, and the inadequacy of stress-point simulations in capturing some intriguing geometrical features of localized deformation. To highlight the main points, we focus for the most part on plane strain simulations. However, we also illustrate a similar trend under triaxial loading condition.

5.1 | Homogeneous rectangular block of Tournemire shale

We consider a rectangular block of overconsolidated Tournemire shale 75 mm tall and 37 mm wide. The finite element mesh is shown in Figure 8A. The sample is subjected to an initial confining pressure of $\sigma_c = 1$ MPa at an initial preconsolidation pressure of $p_c = 40$ MPa, for an overconsolidation ratio of 40. This high overconsolidation ratio extends the range of the elastic response and highlights the role of elastic anisotropy on the ensuing mode of localized failure.

The material parameters for this shale are the same as those given in the previous section. The top and bottom faces are supported on rollers except for one node at the bottom face that is also constrained to move in the horizontal direction to arrest any rigid-body translation mode. Under this condition, the domain deforms homogeneously when the top rollers compress the sample uniformly downwards. What is unusual about the present problem is that, in addition to the domain being compressed vertically, it also swings to the right as a result of elastic anisotropy, as shown in Figure 9. The swing direction is consistent with the weaker, bed-normal direction. The amount by which it swings decreases as the bedding plane orientation decreases, reducing to the value zero when the bedding plane is perfectly horizontal, and the load is perpendicular to it.

Whereas the sample consistently swings in the weaker bed-normal direction throughout the course of the elastic response, the same cannot be said of the swing direction in the plastic range. To fully isolate the elastic and plastic responses, we now set $a = b = 0$ and $\mu_T = \mu_L$ in Equation 11 to obtain an isotropic elastic response. Hence, in this case anisotropy emanates from the plastic response alone. Figure 10 shows that the rotated yield surface produces different swing directions depending on the value of the bedding plane orientation θ . We see that the sample swings to the

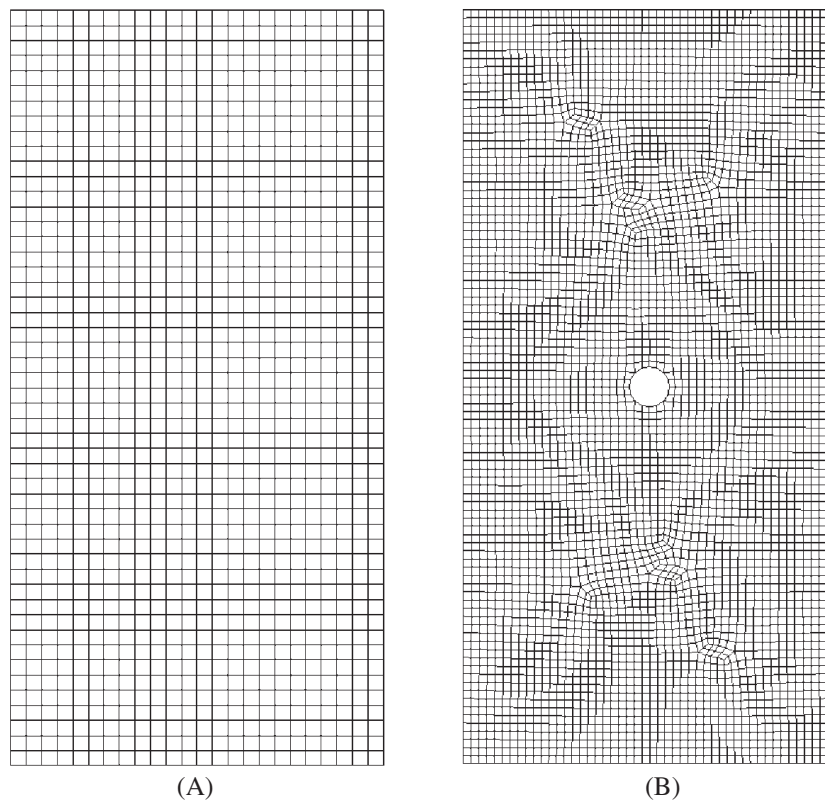


FIGURE 8 Finite element meshes for simulation of plane strain compression of Tournemire shale. A, Homogeneous rock. B, Rock with a hole at the center

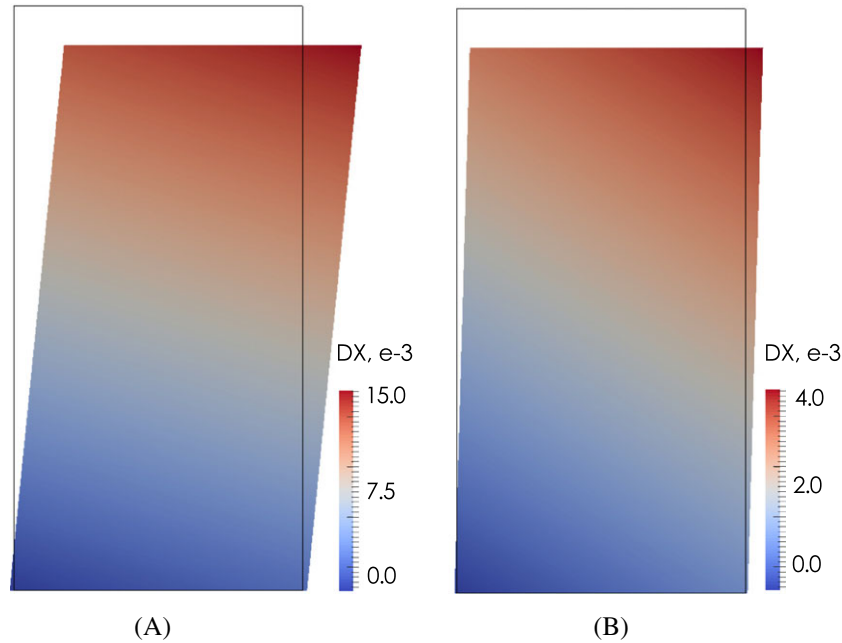


FIGURE 9 Effect of elastic anisotropy on the homogeneous deformation of overconsolidated Tournemire shale. A, $\theta = 45^\circ$. B, $\theta = 15^\circ$. Displacement plots magnification: $500\times$ for u_x and $100\times$ for u_y . Color bars are horizontal displacements in $\text{mm} \times 10^{-3}$ [Colour figure can be viewed at wileyonlinelibrary.com]

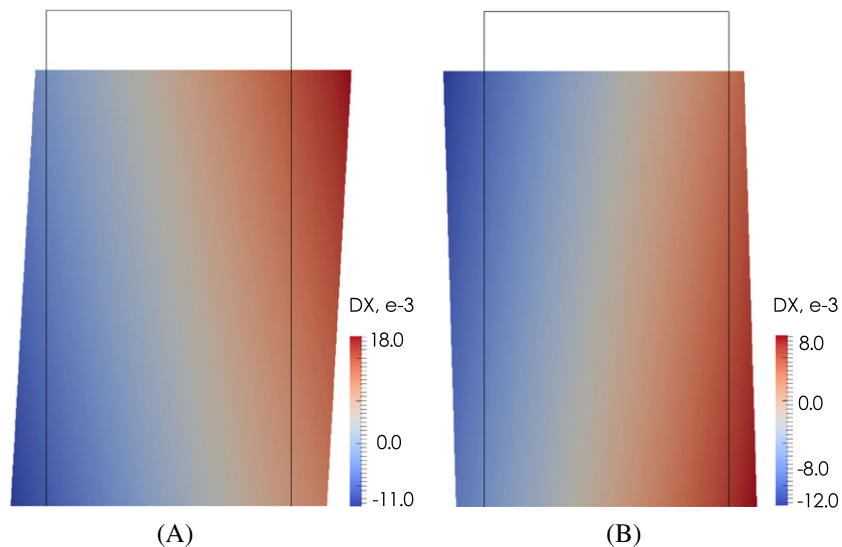


FIGURE 10 Effect of plastic anisotropy on the homogeneous deformation of overconsolidated Tournemire shale. A, $\theta = 45^\circ$. B, $\theta = 15^\circ$. Displacement plots magnification: $500\times$ for u_x and $100\times$ for u_y . Color bars are horizontal displacements in $\text{mm} \times 10^{-3}$ [Colour figure can be viewed at wileyonlinelibrary.com]

right when $\theta = 45^\circ$, and to the left when $\theta = 15^\circ$. Apart from the degree of plastic anisotropy, the swing direction is influenced by the plastic flow direction as well.

The swing direction obviously impacts the structural response when the top and bottom ends are clamped so that the sample is forced to remain vertically aligned throughout the course of loading. The sample in Figure 9A, for example, requires a pair of horizontal forces to move the top end of the sample to the left so that it remains vertically aligned to the bottom end. This results in the development of a zone of localized plastic deformation that runs approximately parallel to the bedding plane, as shown in Figure 11A. On the other hand, the sample shown in Figure 10B requires that this pair of forces move the top end to the right, relative to the bottom end. This results in a localized zone of deformation that runs nearly perpendicular to the bedding plane, as shown in Figure 11B.

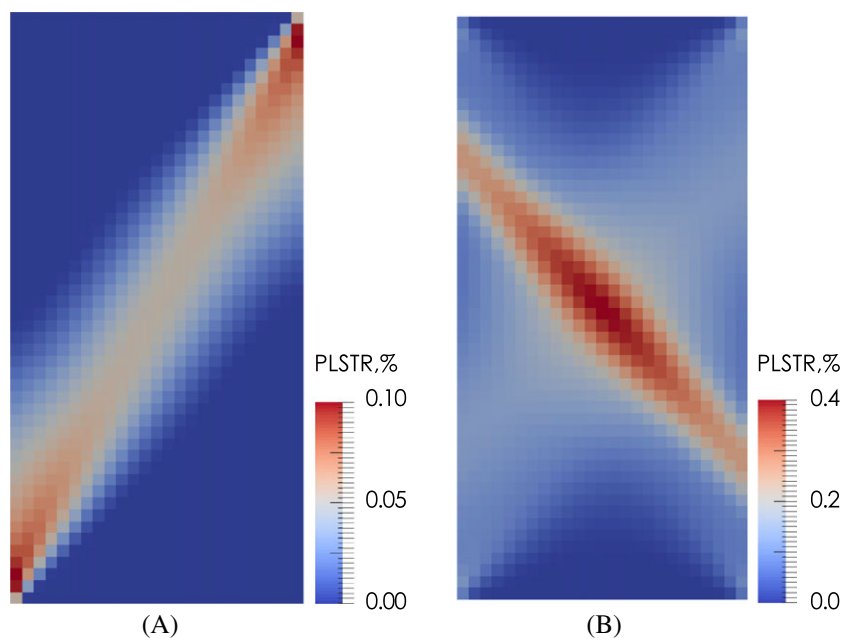


FIGURE 11 Contours of plastic strain $\|\epsilon^p\|$ for plane strain compression of transversely isotropic rocks with clamped ends. A, Shear band in the general direction of the bedding plane produced by elastic anisotropy. B, Shear band nearly perpendicular to the bedding plane produced by plastic anisotropy. Color bars in percent [Colour figure can be viewed at wileyonlinelibrary.com]

When one also considers the effect of local shear band bifurcation, the aforementioned patterns of localized deformation could have important implications for the more complex failure modes observed in transversely isotropic rocks. Consider the failure pattern shown in Figure 11A, for example, in which the general orientation of the localized plastic zone runs in the stronger bed-parallel direction to compensate for swing effect. Yielding on the localized zone results in plastic dilatation and a softening response, followed by local bifurcation into a shear band that runs in the weaker bed-normal direction, according to the results of the previous section.

To avoid the problem of nonunique solution, a common procedure is to introduce enhancements within the localizing element in the form of displacement jumps in the weaker bed-normal direction, upon the detection of local bifurcation.⁶⁰⁻⁶² These element enhancements would act in competition with the global shear band developing from the swing effect along the stronger bed-parallel direction. These competing shear band patterns could explain why failure zones tend to zigzag when the global shear band runs parallel to the bedding plane, as suggested in Figure 12A,B. On the other hand, when the general orientation of the localized plastic zone runs in the bed-normal direction to compensate for swing effect, as shown in Figure 11B, local bifurcation predicts a shear band in the same direction as the plastic zone, so the failure mode does not zigzag but instead remains smooth, as suggested in Figure 12C,D.

5.2 | Rectangular block with a circular hole

Next, we simulate the mechanical response of the same rectangular block of overconsolidated Tournemire shale of the previous example, but now insert a circular hole with a diameter of 4 mm at the center of the block, as shown in the finite element mesh of Figure 8B. It might be useful to compare this example to the acoustic emission tests conducted by Labuz et al⁶³ on a block of Berea sandstone, in which a circular hole was also inserted in the middle of the sample to represent an imperfection, and to the numerical simulations conducted by Borja⁵¹ employing various isotropic plasticity models on a domain with a similar geometric configuration. In the present study, we take the material to be an overconsolidated Tournemire shale with bedding planes oriented at $\theta = 45^\circ$, as in the previous example. The sample is subjected to an outside confining pressure of 1 MPa and an internal pressure of 1 MPa inside the hole.

Figure 13 shows contours of plastic strain generated when the block is compressed vertically assuming smooth ends. With smooth end supports, the block swings freely in the weaker bed-normal direction and, accordingly, develops localized plastic zones emanating from the circular hole and propagating away from it in the weaker bed-normal direction. With the top and bottom ends clamped, however, Figure 14 shows that localized plastic zones emanate from the circular

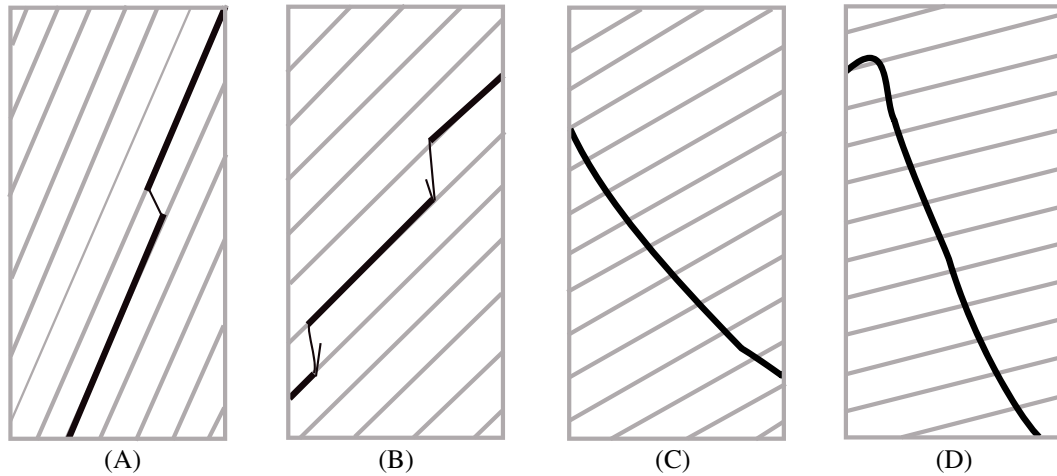


FIGURE 12 Experimentally observed failure modes in synthetic transversely isotropic rocks. After Tien et al²⁴ [Colour figure can be viewed at wileyonlinelibrary.com]

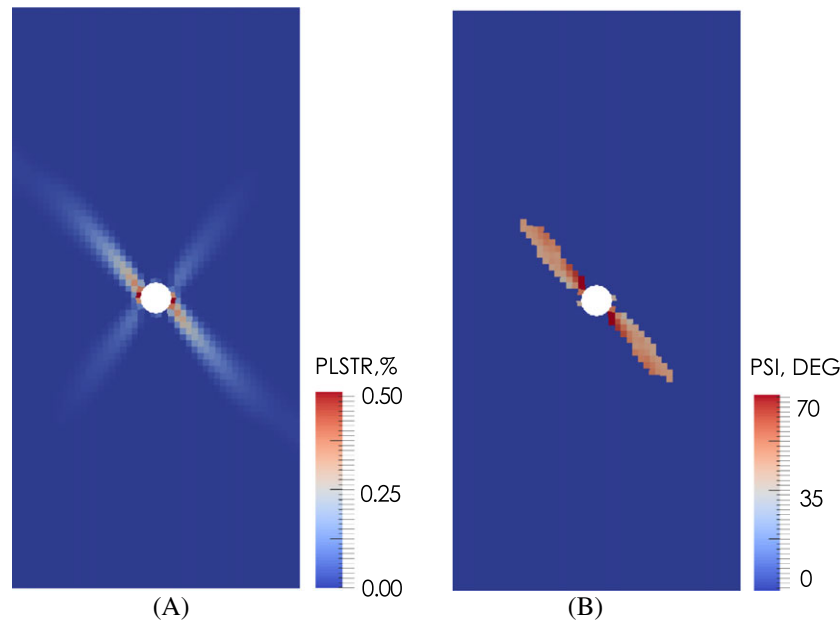


FIGURE 13 Rectangular block with a circular hole and smooth top and bottom ends. A, Contour of plastic strain $\|e^p\|$. B, Contour of shear band angle ψ at bifurcation. Bedding plane orientation is $\theta = 45^\circ$, vertical strain is 0.12% [Colour figure can be viewed at wileyonlinelibrary.com]

hole and propagate away from it in the stronger bed-parallel direction. However, note that secondary bands from local bifurcation still develop from the circular hole and propagate away from it in the weaker bed-normal direction.

5.3 | Three-dimensional simulation of triaxial compression

As a final example, we simulate triaxial tests on a normally consolidated Tournemire shale subjected to a confining pressure of $p_c = \sigma_c = 40$ MPa. The sample is cylindrical with a height of 75 mm and a diameter of 37 mm. The top and bottom ends of the sample are clamped. Axial compression is simulated up to a strain of 2.67%. Two cases with bedding plane orientations $\theta = 30^\circ$ and $\theta = 45^\circ$ have been simulated. Figure 15 depicts the distribution of plastic strain within the cylindrical sample. In both cases, the top and bottom ends of the sample are clamped, and localized zones of plastic deformation develop in the stronger bed-parallel direction to compensate for the swing effect due to both elastic and plastic anisotropy.

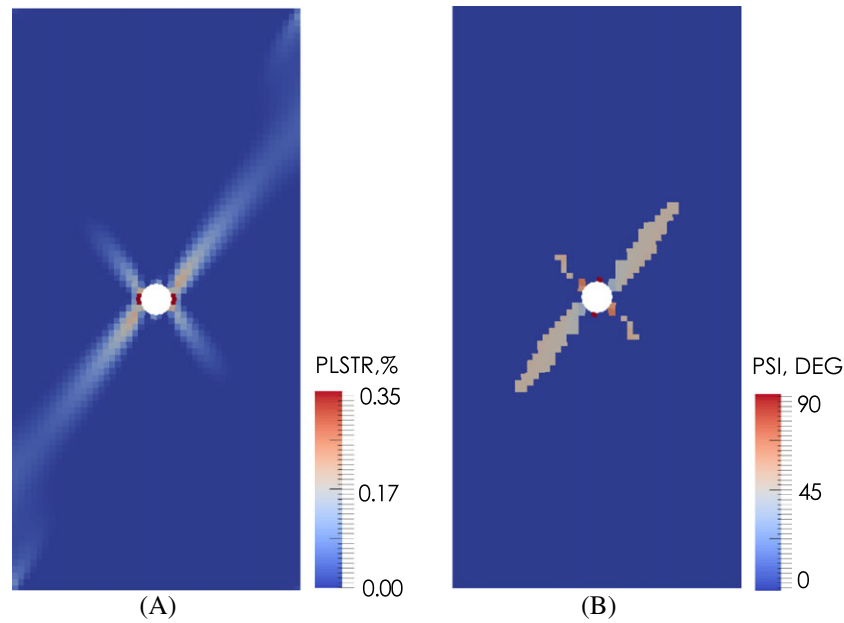


FIGURE 14 Rectangular block with a circular hole and clamped top and bottom ends. A, Contour of plastic strain $\|e^p\|$. B, Contour of shear band angle ψ at bifurcation. Bedding plane orientation is $\theta = 45^\circ$, vertical strain is 0.11% [Colour figure can be viewed at wileyonlinelibrary.com]

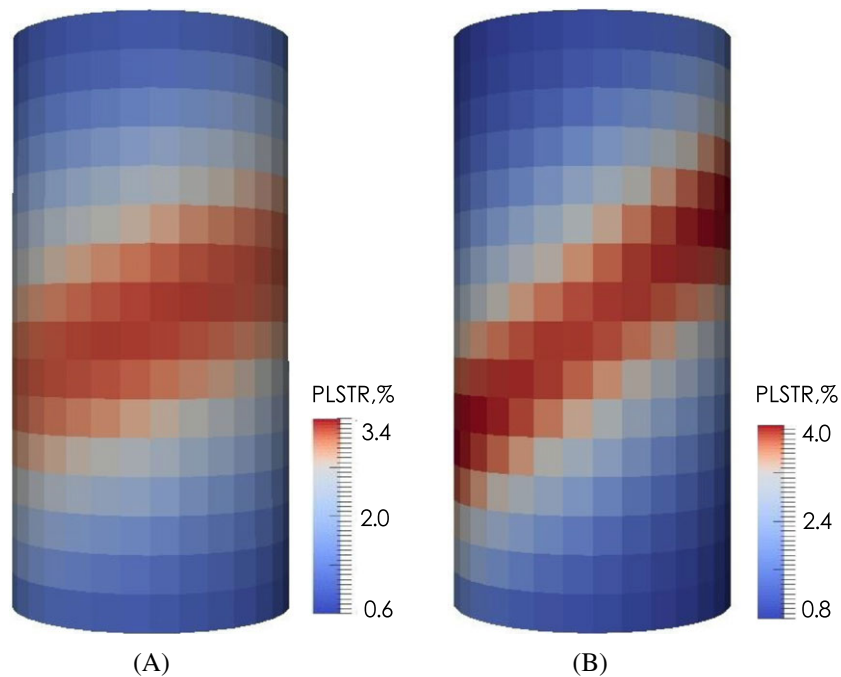


FIGURE 15 Contours of plastic strain $\|e^p\|$ for triaxial compression of normally consolidated Tournemire shale with clamped top and bottom ends. (A) Bedding plane orientation $\theta = 30^\circ$. (B) $\theta = 45^\circ$. Vertical strain is 2.67% [Colour figure can be viewed at wileyonlinelibrary.com]

6 | CLOSURE

The strength of transversely isotropic rocks depends on many factors including the confining pressure, orientation of the bedding plane, overconsolidation ratio of the rock, and temperature. All of these factors have been incorporated into an anisotropic elastoplastic constitutive model based on critical state theory. We have shown that the proposed theory can reproduce the U-shaped variation of rock strength with bedding plane orientation quite well. Yielding on the compression

side results in a competition between compaction-induced hardening and thermal softening; yielding on the dilation side results in a softening response even when the process is isothermal. Whether the rock is yielding on the compression or dilation side, the model predicts an asymmetric U-shaped variation of rock strength with bedding plane orientation.

A novel contribution of this work is the finite element implementation of the aforementioned constitutive theory. Such implementation provides mechanistic insights into processes that cannot be explained with stress-point simulations alone. We have shown how end constraints on a rock sample can reproduce intricate failure zones that zigzag along and across inclined bedding planes. Such complex modes of failure are unique to transversely isotropic materials and cannot be captured by any isotropic plasticity model. We find that for such complicated features of localized deformation, the constitutive model must reflect transverse isotropy in both the elastic and plastic responses. Work in progress includes casting the anisotropic constitutive model into the finite deformation framework, and coupling the solid deformation with a fluid flow model that similarly exhibits transverse isotropy.

ACKNOWLEDGEMENTS

This material is based upon work supported by the U.S. Department of Energy, Office of Science, Office of Basic Energy Sciences, Geosciences Research Program, under Award Number DE-FG02-03ER15454. Support for materials and additional student hours were provided by the National Science Foundation under Award Number CMMI-1462231. The second author acknowledges the National Science Foundation for a Graduate Research Fellowship under grant no. DGE-114747.

ORCID

Ronaldo I. Borja  <http://orcid.org/0000-0002-8877-7468>

REFERENCES

1. Abedi S, Slim M, Ulm F-J. Nanomechanics of organic-rich shales: the role of thermal maturity and organic matter content on texture. *Acta Geotech.* 2016;11(4):775-787.
2. Abedi S, Slim M, Hofmann R, Bryndzia F, Ulm F-J. Nanochemo-mechanical signature of organic-rich shales: a coupled indentation-EDX analysis. *Acta Geotech.* 2016;11(3):559-572.
3. Guo N, Zhao J. Multiscale insights into classical geomechanics problems. *Int J Numer Anal Methods Geomech.* 2016;40(3):367-390.
4. Hu W, Kwok CY, Duan K, Wang T. Parametric study of the smooth-joint contact model on the mechanical behavior of jointed rock. *Int J Numer Anal Methods Geomech.* 2016;42(2):358-376.
5. Kabir P, Ulm F-J, Akono A-J. Rate-independent fracture toughness of gray and black kerogen-rich shales. *Acta Geotech.* 2017;12(6):1207-1227.
6. Li W, Rezakhani R, Jin C, Zhou X, Cusatis G. A multiscale framework for the simulation of the anisotropic mechanical behavior of shale. *Int J Numer Anal Methods Geomech.* 2017;41(14):1494-1522.
7. Liu C, Hoang SK, Abousleiman YN. Responses of chemically active and naturally fractured shale under time-dependent mechanical loading and ionic solution exposure. *Int J Numer Anal Methods Geomech.* 2018;42(1):34-69.
8. Peng P, Ju Y, Wang Y, Wang S, Gao F. Numerical analysis of the effect of natural microcracks on the supercritical CO₂ fracturing crack network of shale rock based on bonded particle models. *Int J Numer Anal Methods Geomech.* 2017;41(18):1992-2013.
9. Wong LNY, Maruvanchery V, Liu G. Water effects on rock strength and stiffness degradation. *Acta Geotech.* 2016;11(4):713-737.
10. Wu H, Guo N, Zhao J. Multiscale modeling and analysis of compaction bands in high-porosity sandstones. *Acta Geotech.* 2018;13(3):575-599.
11. Zhang P, Lin G, Liu J, Wang W. Response of multilayered transversely isotropic medium due to axisymmetric loads. *Int J Numer Anal Methods Geomech.* 2016;40(6):827-864.
12. Abousleiman YN, Hull KL, Han Y, et al. The granular and polymer composite nature of kerogen-rich shale. *Acta Geotech.* 2016;11(3):573-594.
13. Donath FA. Experimental study of shear failure in anisotropic rocks. *Geol Soc Am Bull.* 1961;72(6):985-989.
14. Hoek E. Fracture of anisotropic rock. *J South Afr Inst Min Metall.* 1964;64(10):501-523.
15. Attewell PB, Sandford MR. Intrinsic shear strength of a brittle, anisotropic rock-I: experimental and mechanical interpretation. *Int J Rock Mech Min Sci Geomech Abstr.* 1974;11(11):423-430.
16. McLamore R, Gray KE. The mechanical behavior of anisotropic sedimentary rocks. *J Eng Ind Trans.* 1967;89(1):62-73.
17. Bonnelye A, Schubnel A, David C, et al. Strength anisotropy of shales deformed under uppermost crustal conditions. *J Geophys Res Solid Earth.* 2017;122(1):110-129.
18. Niandou H, Shao JF, Henry JP, Fourmaintraux D. Laboratory investigation of the mechanical behaviour of Tournemire shale. *Int J Rock Mech Min Sci.* 1997;34(1):3-16.
19. Ramamurthy T, Rao GV, Singh J. Engineering behaviour of phyllites. *Eng Geol.* 1993;33(3):209-225.

20. Nasser MHB, Rao KS, Ramamurthy T. Anisotropic strength and deformational behavior of Himalayan schists. *Int J Rock Mech Min Sci.* 2003;40(1):3-23.
21. Bennett KC, Berla LA, Nix WD, Borja RI. Instrumented nanoindentation and 3D mechanistic modeling of a shale at multiple scales. *Acta Geotech.* 2015;10:1-14.
22. Harris NB, Miskimins JL, Mnich CA. Mechanical anisotropy in the Woodford Shale, Permian Basin: origin, magnitude, and scale. *Lead Edge.* 2011;30(3):284-291.
23. Semnani SJ, Borja RI. Quantifying the heterogeneity of shale through statistical combination of imaging across scales. *Acta Geotech.* 2017;12:1193-1205.
24. Tien YM, Kuo MC, Juang CH. An experimental investigation of the failure mechanism of simulated transversely isotropic rocks. *Int J Rock Mech Min Sci.* 2006;43(8):1163-1181.
25. Tien YM, Kuo MC. A failure criterion for transversely isotropic rocks. *Int J Rock Mech Min Sci.* 2001;38(3):399-412.
26. Duveau G, Shao JF, Henry JP. Assessment of some failure criteria for strongly anisotropic geomaterials. *Mech Cohesive-Frictional Mater.* 1998;3(1):1-26.
27. Duveau G, Shao JF. A modified single plane of weakness theory for the failure of highly stratified rocks. *Int J Rock Mech Min Sci.* 1998;35(6):807-813.
28. Jaeger JC. Shear failure of anisotropic rocks. *Geol Mag.* 1960;97(1):65-72.
29. Walsh JB, Brace WF. A fracture criterion for brittle anisotropic rock. *J Geophys Res.* 1964;69(16):3449-3456.
30. Hoek E, Brown ET. Empirical strength criterion for rock masses. *J Geotech Geoenviron.* 1980;106(ASCE 15715).
31. Ramamurthy T. Strength and modulus responses of anisotropic rocks. *Compreh rock eng.* 1993;1(13):313-329.
32. Saroglou H, Tsiambaos G. A modified Hoek–Brown failure criterion for anisotropic intact rock. *Int J Rock Mech Min Sci.* 2008;45(2):223-234.
33. Jaeger JC. Friction of rocks and stability of rock slopes. *Geotechnique.* 1971;21(2):97-134.
34. Gol'denblat II, Kopnov VA. Strength of glass-reinforced plastics in the complex stress state. *Mech Compos Mater.* 1965;1(2):54-59.
35. Tsai SW, Wu EM. A general theory of strength for anisotropic materials. *J Compos Mater.* 1971;5(1):58-80.
36. Hill R. A theory of the yielding and plastic flow of anisotropic metals; In: Proceedings of the Royal Society of London A: Mathematical, Physical and Engineering Sciences;1948:281-297.
37. Pariseau WG. Plasticity theory for anisotropic rocks and soil. In: The 10th US Symposium on Rock Mechanics (USRMS); 1968:20-22.
38. Boehler JP, Sawczuk. A On yielding of oriented solids. *Acta Mechanica.* 1977;27(1-4):185-204.
39. Nova R. The failure of transversely isotropic rocks in triaxial compression. *International Journal of Rock Mechanics and Mining Sciences and Geomechanics Abstracts.* 1980:325-332.
40. Crook AJ, Yu JG, Willson SM. Development of an orthotropic 3D elastoplastic material model for shale. In: SPE/ISRM Rock Mechanics Conference; 2002; Irving, Texas.
41. Semnani SJ, White JA, Borja RI. Thermo-plasticity and strain localization in transversely isotropic materials based on anisotropic critical state plasticity. *Int J Numer Anal Methods Geomech.* 2016;40:2423-2449.
42. Borja RI, Rahmani H. Computational aspects of elasto-plastic deformation in polycrystalline solids soils. *J Appl Mech.* 2012;79(3):031024.
43. Borja RI, Rahmani H. Discrete micromechanics of elastoplastic crystals in the finite deformation range. *Comput Methods Appl Mech Eng.* 2014;275:234-263.
44. Tjioe M, Borja RI. On the pore-scale mechanisms leading to brittle and ductile deformation behavior of crystalline rocks. *Int J Numer Anal Methods Geomech.* 2015;39(11):1165-1187.
45. Tjioe M, Borja RI. Pore-scale modeling of deformation and shear band bifurcation in porous crystalline rocks. *Int J Numer Methods Eng.* 2016;108(3):183-212.
46. Hueckel T, Baldi G. Thermoplasticity of saturated clays: experimental constitutive study. *J Geotech Eng.* 1990;116(12):1778-1796.
47. Masri M, Sibai M, Shao JF, Mainguy M. Experimental investigation of the effect of temperature on the mechanical behavior of Tournemire shale. *Int J Rock Mech Min Sci.* 2014;70:185-191.
48. Mohamadi M, Wan RG. Strength and post-peak response of Colorado shale at high pressure and temperature. *Int J Rock Mech Min Sci.* 2016;84:34-46.
49. Hueckel T, Borsetto M. Thermoplasticity of saturated soils and shales: constitutive equations. *J Geotech Eng.* 1990;116(12):1765-1777.
50. Graham J, Tanaka N, Crilly T, Alfaro M. Modified Cam-Clay modelling of temperature effects in clays. *Can Geotech J.* 2001;38(3):608-621.
51. Borja RI. *Plasticity Modeling & Computation.* Berlin-Heidelberg: Springer; 2013.
52. Laloui L, Cekerevac C. Thermo-plasticity of clays: an isotropic yield mechanism. *Comput Geotech.* 2003;30(8):649-660.
53. Borja RI. Bifurcation of elastoplastic solids to shear band mode at finite strain. *Comput Methods Appl Mech Eng.* 2002;191(146):5287-5314.
54. Rudnicki JW, Rice JR. Conditions for the localization of deformation in pressure-sensitive dilatant materials. *J Mech Phys Solids.* 1975;23(6):371-394.
55. Bennett KC, Borja RI. Hyper-elastoplastic/damage modeling of rock with application to porous limestone. *Int J Solids Struct.* 2018. <https://doi.org/10.1016/j.ijsolstr.2018.03.011>
56. Bennett KC, Regueiro RA, Borja RI. Finite strain elastoplasticity considering the Eshelby stress for materials undergoing plastic volume change. *Int J Plast.* 2016;77:214-245.

57. Borja RI, Aydin A. Computational modeling of deformation bands in granular media, I: Geological and mathematical framework. *Comput Methods Appl Mech Eng.* 2004;193(27–29):2667-2698.
58. Borja RI. Computational modeling of deformation bands in granular media, II: Numerical simulations. *Comput Methods Appl Mech Eng.* 2004;193(27–29):2699-2718.
59. Backus GE. Long-wave elastic anisotropy produced by horizontal layering. *J Geophys Res.* 1962;67(11):4427-4440.
60. Borja RI. A finite element model for strain localization analysis of strongly discontinuous fields based on standard Galerkin approximations. *Comput Methods Appl Mech Eng.* 2000;190(11–12):1529-1549.
61. Regueiro RA, Borja RI. Plane strain finite element analysis of pressure-sensitive plasticity with strong discontinuity. *Int J Solids Struct.* 2001;38(21):3647-3672.
62. Liu F, Borja RI. A contact algorithm for frictional crack propagation with the extended finite element method. *Int J Numer Methods Eng.* 2008;78(10):1489-1512.
63. Labuz JF, Riedel JJ, Dai ST. Shear fracture in sandstone under plane-strain compression. *Eng Fract Mech.* 2006;73:820-828.

How to cite this article: Zhao Y, Semnani SJ, Yin Q, Borja RI. On the strength of transversely isotropic rocks. *Int J Numer Anal Methods Geomech.* 2018;42:1917–1934. <https://doi.org/10.1002/nag.2809>

APPENDIX A : BACKUS AVERAGE

The stress-strain relationship for a linear elastic material can be written in matrix form as follows:

$$\{\sigma\} = [C^e]\{\epsilon^e\}, \quad (A1)$$

where $\{\sigma\} = \{\sigma_{11} \ \sigma_{22} \ \sigma_{33} \ \sigma_{23} \ \sigma_{13} \ \sigma_{12}\}^T$ and $\{\epsilon^e\} = \{\epsilon_{11}^e \ \epsilon_{22}^e \ \epsilon_{33}^e \ \gamma_{23}^e \ \gamma_{13}^e \ \gamma_{12}^e\}^T$ are vector representations of the stress tensor and elastic strain tensor, respectively; $[C^e]$ is the matrix representation of the linear elastic tangent. For a transversely isotropic material whose symmetry axis is $\{1 \ 0 \ 0\}^T$, $[C^e]$ could be expressed as follows:

$$[C^e] = \begin{bmatrix} c_{11} & c_{12} & c_{12} & 0 & 0 & 0 \\ c_{12} & c_{33} & c_{13} & 0 & 0 & 0 \\ c_{12} & c_{13} & c_{33} & 0 & 0 & 0 \\ 0 & 0 & 0 & c_{66} & 0 & 0 \\ 0 & 0 & 0 & 0 & c_{44} & 0 \\ 0 & 0 & 0 & 0 & 0 & c_{44} \end{bmatrix}. \quad (A2)$$

For a layered transversely isotropic material, Backus⁵⁹ proposed an average method to calculate its effective elastic tangent. The 6 components of $[C^e]$ can be calculated as follows:

$$\begin{aligned} c_{11} &= \langle H^{-1} \rangle^{-1} \\ c_{12} &= \langle H^{-1} \rangle^{-1} \left\langle \frac{H - 2\mu}{H} \right\rangle \\ c_{13} &= \langle H^{-1} \rangle^{-1} \left\langle \frac{H - 2\mu}{H} \right\rangle^2 + 2 \left\langle \frac{(H - 2\mu)\mu}{H} \right\rangle \\ c_{44} &= \langle \mu^{-1} \rangle^{-1} \\ c_{66} &= \langle \mu \rangle \\ c_{33} &= c_{13} + 2c_{66}, \end{aligned} \quad (A3)$$

where $H = K + \frac{4}{3}\mu$, K and μ are the elastic bulk and shear moduli, respectively; $\langle \cdot \rangle$ refers to Voigt average of the content weighted by the thickness of each layer.